Article

High-Sensitivity Temperature Sensor Based on the Perfect Metamaterial Absorber in the Terahertz Band

Yan Wang [1], Yanqing Qiu [1], Yingping Zhang [1], Tingting Lang [2],* and Fengjie Zhu [3],*

[1]   Institute of Optoelectronic Technology, China Jiliang University, Hangzhou 310018, China
[2]   School of Information and Electronic Engineering, Zhejiang University of Science and Technology, Hangzhou 310023, China
[3]   The First School of Clinical Medicine, Zhejiang Chinese Medical University, Hangzhou 310003, China
*   Correspondence: langtingting@zust.edu.cn (T.L.); 20071010@zcmu.edu.cn (F.Z.)

Abstract: In this study, a perfect metamaterial absorber (PMMA) based on an indium antimonide temperature-sensitive material is designed and investigated in the terahertz region. We demonstrate that it is an ideal perfect narrow-band absorber with polarization-insensitive and wide-angle absorption properties. Numerical simulation results show that the proposed PMMA can be operated as a temperature sensor with a sensitivity of 21.9 GHz/K. A graphene layer was added to the PMMA structure to improve the sensitivity, and the temperature sensitivity was increased to 24.4 GHz/K. Owing to its excellent performance, the proposed PMMA can be applied in thermal sensing, detection, and switching.

Keywords: perfect absorber; temperature sensor; metamaterials; terahertz

1. Introduction

Terahertz (THz) waves refer to electromagnetic waves with frequencies between 0.1 and 10 THz, which are between infrared and microwaves in the electromagnetic spectrum. This particular location provides some of the properties of both microwaves and light waves. In addition, it has some characteristics that are different from other bands of electromagnetic waves, such as fingerprint spectrum characteristics, high penetration, low photon energy, and anti-interference ability, which makes THz technology attractive. In recent years, THz technology has rapidly developed and has been applied in wireless communication [1], biomedicine [2], imaging [3], and sensing [4]. Metamaterials are artificial electromagnetic media constructed on a subwavelength scale [5]. The flexible control of different modes of electromagnetic wave action by metamaterials is realized through the ingenious design of the unit structure of electromagnetic metamaterials. We combine THz with metamaterial technology to realize space optical sensing. Compared with the traditional temperature detection method, it is a passive and wireless sensing method. Moreover, the temperature sensor also has many other advantages, such as its high sensitivity, remote measurement, high penetration, little damage, wide range of temperature measurement, micro-integration, and so on.

Numerous modern temperature sensors rely on the resistance measurement of thin metal films or wires, whose resistance varies with temperature [6]. In recent years, optical sensors have drawn the attention of many researchers because of their high sensitivity, high resolution, small size, high stability, high linearity, and resistance to mechanical shock and electromagnetic interference. Various types of optical temperature sensors were reported, including optical waveguides [7–11], optical fibers [12–14], metamaterials [15–17], ring resonators [18,19], and fluorescent materials [20,21]. For example, Guan et al. proposed a sensor made of a silicon/polymer hybrid waveguide with a sensitivity of 172 pm/°C (~25.5 GHz/°C) at 1550 nm (193.5 THz) [7]. Wei Q. et al. proposed a nano-scale temperature sensor based on Fano resonance with a temperature sensitivity of 360 pm/°C

(~71.8 GHz/°C) at 1250 nm(240 THz) [10]. Karim proposed a metamaterial temperature sensor comprising a closed-loop resonator array embedded in a matrix of dielectric materials with a sensitivity of 0.462 MHz/°C at 12 GHz [15]. Radhouene et al. proposed a temperature sensor based on the transmission of a two-dimensional photonic crystal (PC) superelliptical ring resonator with a structured sensitivity of 65.3 pm/°C (~8.4 GHz/°C) at 1550 nm (193.5 THz) [18]. Xia proposed a non-contact optical temperature measurement technology based on the fluorescence intensity ratio (FIR), and the calculated relative sensitivity over the entire measurement temperature range exceeded 1.08%/K at 600 nm (500 THz) [20].

Among the temperature sensors, metals, dielectrics, polymers, and other materials are used, and the combined characteristics of the thermo-optical and thermal expansion effects of the materials are used to achieve temperature-dependent changes [22]. Moreover, some temperature-sensitive materials based on other models were studied, such as strontium titanate oxide, based on the damped harmonic oscillator model [23,24]; graphene, based on Falkovsky's formula [25,26]; InSb, based on the Drude model [27–30]; vanadium dioxide temperature phase-change material [31]; and fluorine crown based on the Sellmaier equation [32]. Among semiconductors, InSb has been widely studied because it has a smaller band gap than other semiconductors and is more sensitive to temperature. For example, Luo et al. proposed a temperature-sensing tunable THz dual-frequency perfect absorber based on a combined InSb resonator structure; the sensitivity reaches 7144 nm/K(~4 GHz/K) at 0.3–0.6 THz [16]. Zou Haijun proposed the design of a six-band THz metamaterial absorber for temperature sensing with a temperature sensitivity of up to 10.3 GHz/K at 0.4–2.2 THz [27]. In addition, the optical properties of graphene materials depend on temperature. Owing to its high mobility, optical transparency, flexibility, robustness, and environmental stability [33–37], it has been incorporated into many metamaterial structures for application in thermophotovoltaic devices.

In this study, we proposed a perfect THz metamaterial absorber based on the semiconductor InSb. We demonstrated that the absorber can achieve an absorption rate of 99.9% in the THz region. The surface current and electromagnetic field distributions of the unit structure were studied to better understand the physical mechanism of the proposed perfect metamaterial absorber (PMMA). In addition, the polarization insensitivity and wide-angle absorption properties of this structure were demonstrated. The effects of different structural parameters on the absorption properties of the proposed PMMA were analyzed. The designed PMMA can be used in high-sensitivity passive wireless optical temperature sensors and thermal switch applications. The numerical simulation results show that when the external temperature changes from 260 to 310 K, the resonance peak shifts from 2.047 to 3.141 THz, and the temperature sensitivity reaches 21.9 GHz/K. The use of both semiconductors and graphene in the PMMA structure was proposed to improve the sensitivity. By adding a graphene layer, the temperature sensitivity increased to 24.4 GHz/K. Furthermore, the effects of the top circular radius R and thickness t of the InSb layer on the sensitivity of PMMA were investigated.

2. Materials and Methods

A unit structure diagram of PMMA is shown in Figure 1. As shown in Figure 1a, the structures from top to bottom along the *z*-axis are the top circular metal pattern layer, InSb dielectric layer, metal layer, and quartz substrate. Figure 1b shows the top view of the unit cell. The unit period was $P_x = P_y = 50$ μm, and the top circular radius (R) was 16 μm. The side view is shown in Figure 1c. The thickness of the InSb dielectric layer is $H = 3$ μm. The top and bottom metal layers are copper with a conductivity of 5.7×10^7 S/m, and their thicknesses, t_1 and t_2, are both 0.4 μm. A quartz substrate was used as the support for the superstructure. In the simulation, the substrate was set to 30 μm thick, and the dielectric constant was 3.78.
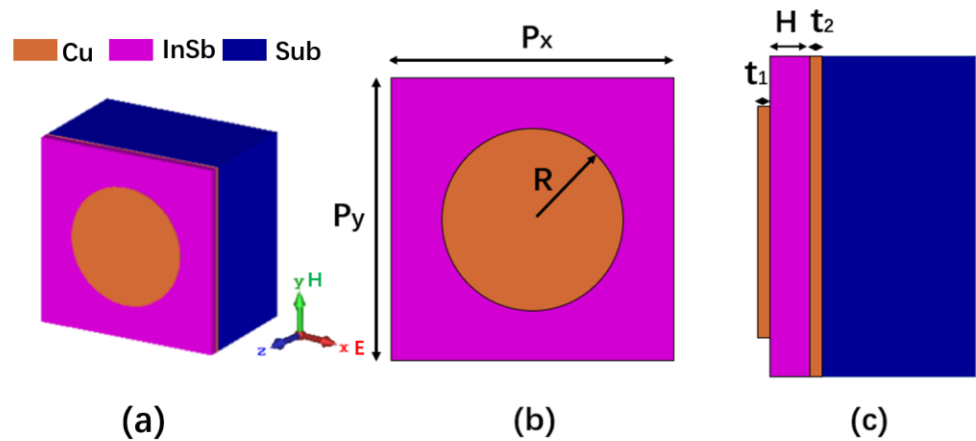
Figure 1. (**a**) Unit structure diagram of the proposed absorber, (**b**) top view of unit cell structure, (**c**) side view of unit cell structure. The structure parameters are: $Px = Py = 50$ μm, $R = 16$ μm, $H = 3$ μm, $t_1 = t_2 = 0.4$ μm.

Full-wave simulations were conducted based on the finite element method using CST Microwave Studio to explore the temperature characteristics and gain a deep understanding of the physical principles of PMMA. The simulation frequency range is $1.5-3.5$ THz, the plane wave is perpendicular to the unit structure, and the electric field is parallel to the *x*-axis (TM mode). A perfectly matched layer is used along the z-direction, periodic boundary conditions are used along the x- and y-directions, cells per max model box edge is set to 10, minimum cell is set to absolute value 0, and meshing method is set to Default (surface-based). The absorption rate A of the metamaterial absorber can be obtained as $A = 1 - T - R$, where T and R are the transmission and reflection, respectively. Because the thickness of the metal film layer is greater than the skin depth of the incident beam, transmittance T should be close to zero. Therefore, the absorption rate A can be simplified to $A = 1 - R$. Simultaneously, if R is close to zero, PMMA can achieve complete absorption.

Since semiconductors are materials with a small band gap, small temperature changes result in the transfer of electrons between the bands. Therefore, semiconductors are highly sensitive to temperature variations. Among the semiconductors, InSb, due to its small band gap than the rest of the semiconductors, is more sensitive to temperature. Therefore, it is selected as the temperature-sensing material. It can emulate a metal in the THz regime, supports the transmission of surface plasmon waves [38,39], and has the characteristics of narrow band gap, high electron mobility, and low electron density in the THz band [40]. The complex-valued relative permittivity of InSb at different temperatures can be calculated using the Drude model [41–43]:

$$\varepsilon(\omega, T) = \varepsilon_\infty - \frac{\omega_p{}^2(T)}{\omega[\omega + i\gamma]} \tag{1}$$

where ε_∞ is the high-frequency value ($\varepsilon_\infty = 15.68$), ω is the angular frequency, T is the thermodynamic temperature (in Kelvin), γ is the damping constant ($\gamma = 0.1\,\pi$ THz) [44], and $\omega_p(T)$ is the plasma frequency, which represents the natural frequency of freely oscillating conduction electrons, and can be described by the following relationship:

$$\omega_p(T) = \sqrt{(e^2 N_d(T))/(\varepsilon_0 m^*)} \tag{2}$$

where the free space permittivity ε_0 is 8.854×10^{-12} F/m, m^* is the effective mass of the electron with a value of $0.015 me$ ($me = 9.108 \times 10^{-31}$ kg), and e is the electron charge (1.602×10^{-19} C). The intrinsic carrier concentration is expressed as $N_d(T) = 5.76 \times 10^{14} T^{1.5} exp(-0.13/k_B T)$ cm^{-3} [45], where K_B is Boltzmann's constant, and T is the temperature.

Thus, the temperature dependence of InSb can be attributed fundamentally to the increase in intrinsic carrier concentration by thermal excitation as the temperature increase. As shown in Figure 2, the real and imaginary parts of the dielectric constant of InSb at different temperatures can be calculated using the above formula, which is highly consistent with the results in previous articles [27–29]. It can be observed that the relative permittivity $\varepsilon(\omega)$ of InSb can be dynamically adjusted by changing the temperature T. In order to visually compare the temperature dependence of different materials, the complex-valued relative permittivity of InSb is quantified into the thermo-optical coefficient, which is calculated as $-7.7 \times 10^{-3} \text{ K}^{-1}$. Therefore, we expect that the InSb temperature change can influence the absorption characteristics of the proposed PMMA.
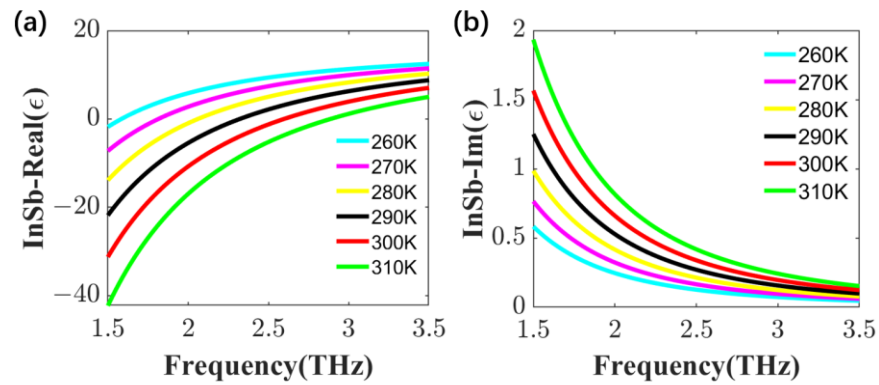

Figure 2. Real (**a**) and imaginary (**b**) parts of the dielectric constant of InSb at different temperatures.

In the THz region, the optical properties of graphene also depend on temperature [26]. As Keshavarz proposed that the spectral shifts induced by the temperature change of InSb and graphene are in the same direction [17], it can be speculated that if both of them are present in the sensor structure, the sensitivity will increase significantly. Therefore, we employed a combination of the absorber structure and graphene to improve the temperature sensitivity.

In this study, according to the Kubo formula [46,47], the electrical conductivity of graphene can be calculated as the sum of the interband σ_{inter} and intraband σ_{intra} contributions using the formula: $\sigma = \sigma_{inter} + \sigma_{intra}$, in which

$$\sigma_{inter} = \frac{e^2}{4\hbar}\left[\frac{1}{2} + \frac{1}{\pi}\arctan\left(\frac{\hbar\omega - 2\mu}{2k_B T}\right)\right] - \frac{e^2}{4\hbar}\left[\frac{i}{2\pi}ln\frac{(\hbar\omega - 2\mu)^2}{(\hbar\omega - 2\mu)^2 + (2k_B T)^2}\right] \quad (3)$$

$$\sigma_{intra} = \frac{2ie^2 k_B T}{\pi\hbar^2(\omega + i\tau)}ln\left[2\cos h\frac{\mu}{2k_B T}\right] \quad (4)$$

here, e is the charge of the electron, $\hbar$ is the reduced Planck constant, K_B is Boltzmann's constant, T is the temperature, τ is the carrier momentum relaxation time (scattering time), μ is the chemical potential, and ω is the angular frequency. In terahertz frequency, in which $\hbar\omega \ll \mu$, the contribution of intraband interaction is significant so that σ_{intra} dominates the contribution to graphene conductivity. The permittivity of the graphene was obtained using the following Equation:

$$\varepsilon_g = 1 + i\frac{\sigma_g}{\varepsilon_0\omega\Delta} \quad (5)$$

where Δ is the thickness of the graphene in the structure and ε_0 is the permittivity of free space. We consider that the single-layer chemical vapor deposition graphene layer is a thin graphene sheet, and thus it is equivalent to a two-dimensional impedance sheet in the simulation.

As described above, it can be observed that graphene has temperature dependence. We use "Create Graphene Material" under the "Macros" menu to simulate graphene with

the following parameters of graphene in the simulation: Δ = 1 nm, τ = 0.1 ps [48], μ = 0.0 eV, and set different temperature T parameters. In our later research, a graphene thin-film layer is placed between the InSb layer and the top metal layer. Similarly, the real and imaginary parts of the intraband electrical conductivity of graphene at different temperatures can be calculated according to Formula (4), as shown in Figure 3. Although the effect of temperature is not as large as that for the InSb material, it can be proved that temperature can affect the conductivity of graphene and then affect the resonance frequency.
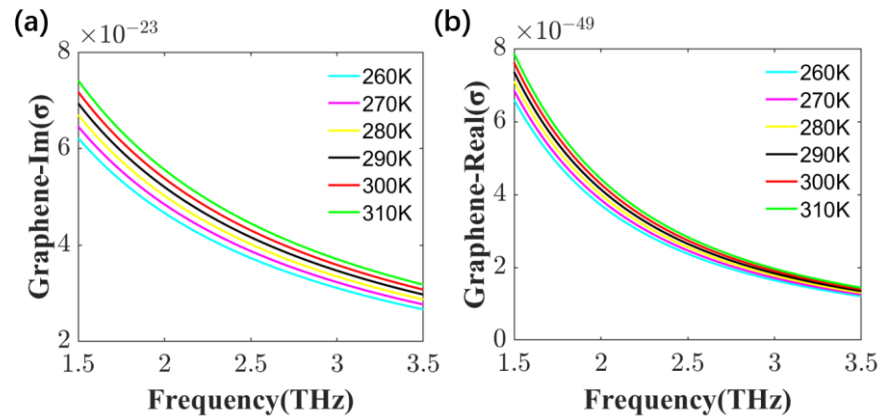

Figure 3. Real (**a**) and imaginary (**b**) parts of the intraband electrical conductivity of graphene at different temperatures.

For the fabrication of the metamaterial structure, first, a thin film of copper to be plated on the quartz substrate by chemical vapor deposition (CVD), and a single-side polished InSb substrate is further bonded to the quartz substrate using an epoxy resin adhesive. Then, the InSb substrate is thinned and polished to obtain the InSb thin layer. The metal copper film continues to grow on InSb thin layer at low temperatures by CVD. The top pattern layer is fabricated by the semiconductor etching process of wet etching. Finally, the entire metamaterial structure is obtained.

3. Results and Discussion

3.1. Spectrum

Figure 4 shows the simulated reflection, transmission, and absorption spectra of the proposed PMMA when the external temperature T was 280 K. It can be observed that the transmission is zero in the entire relevant frequency range. As shown in Figure 4, there is an obvious absorption peak at 2.426 THz, with an absorption rate of 99.9%. At this point, the intrinsic carrier concentration of InSb N_d = 1.240 × 1022 m^{-3}, the plasma frequency ω_p = 5.129 × 10^{13} rad/s, the real and imaginary parts of the dielectric constant of InSb is Real(ε) = 4.361 and Image(ε) = 0.233. In particular, the structure has a narrow bandwidth, and the full width at half maximum (*FWHM*) is only 0.08 THz, which makes the structure show remarkable sensing properties. The quality factor Q ($Q = f_0/FWHM$) of the resonant absorption peak was 30. An ideal absorber has strong frequency selectivity owing to its narrow absorption bandwidth and large absorption coefficient.
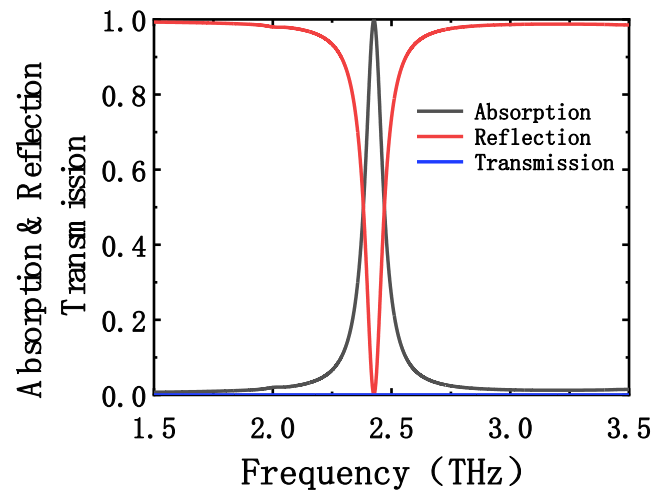
Figure 4. Simulated reflection, transmission, and absorption spectra of the proposed PMMA when the external temperature *T* is 280 K.

3.2. Properties

We then investigated the sensitivity of the proposed PMMA to the polarization and incidence angle of THz waves. Figure 5a,c shows the dependence between the absorbance spectrum and polarization angle between 0 and 90° under normal incident waves in the TM mode and TE mode, respectively. Owing to the good symmetry of the proposed PMMA structure, different polarization angles (0–90°) of the normally incident THz wave do not affect the absorption performance. The results revealed that the absorption spectrum of PMMA is independent of the polarization angle.
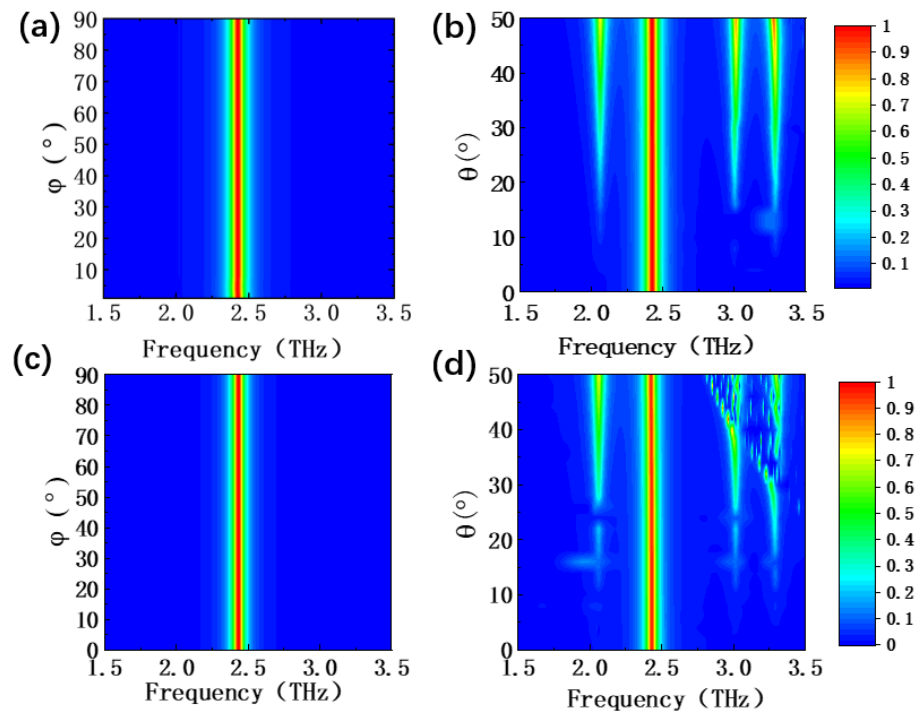

Figure 5. Simulated absorbance spectrum of the proposed PMMA with different (**a**) polarization and (**b**) incident angles in the TM mode and in the TE mode(**c**,**d**) when T = 280K.

Next, the absorption effect of the designed PMMA with incidence angles from 0 to 50° in the TM mode and TE mode was also considered. As shown in Figure 5b,d, no matter whether in TM mode or TE mode, with an increase in the incident angle, the

strong absorption performance at the absorption peak (f = 2.426 THz) remains unchanged, and there is no frequency shift, which is beneficial for the sensor to reduce error and calibration complexity. When the incident angle was greater than 20°, spurious peaks appeared because higher-order resonances were induced as the incident angle increased. The simulated absorbance spectrum of TE mode with different incident angles is slightly different from that of TM mode, and its spurious peaks are distributed more irregularly. However, in this case, the main absorption peak characteristics were unaffected. When the incident angle is greater than 50°, it can be inferred that the absorption rate of the fourth peak will gradually approach 100%. Considering that this will cause misjudgment of the characteristic peak, we suppose that PMMA has a good absorption peak when the incident angle is less than 50°. In summary, the designed PMMA exhibited polarization insensitivity and wide-angle absorption properties.

3.3. Principle

To explain the resonance absorption principle of PMMA, we observed and analyzed the surface current and electric and magnetic field distributions with the incident THz wave perpendicular to the PMMA cell structure in the TM mode at the resonance frequency (f = 2.426 THz). As can be observed in Figure 6c, massive charges are accumulated on both sides of the metal circle, forming a highly enhanced electric field. As shown in Figure 6d, these accumulated charges also excite corresponding mirror charges with opposite signs on the metallic-backed layer, resulting in an enhanced electric field in the InSb dielectric layer. At the same time, these accumulated charges in the metal circular and the metallic backed layer oscillate with the variation of the incident electric field, forming a pair of antiparallel currents in the two metal layers and displacement currents in the dielectric layer. The antiparallel current and the displacement current constitute a closed loop, inducing a magnetic dipole. Among them, the antiparallel currents can be seen in Figure 6a,b, and the magnetic dipole can be seen in Figure 6e,f. The magnetic dipole interacts with the magnetic field component of the incident wave and produces a magnetic dipole resonance. Finally, the electromagnetic energy of the incident wave is bound in the absorber structure and is lost as heat or other forms of energy so that the electromagnetic wave can be completely absorbed.
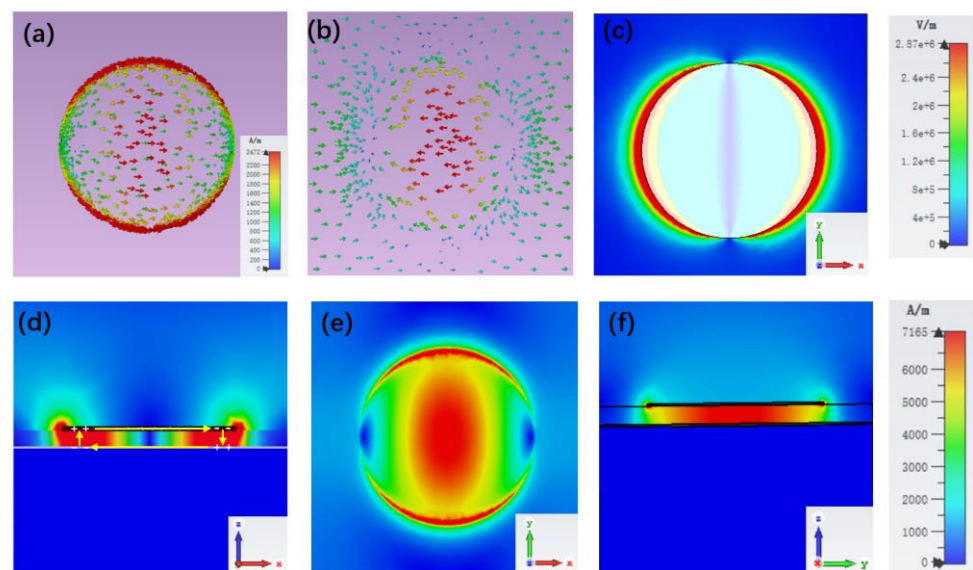

Figure 6. Distributions of the surface current of (**a**) the top metal layer and (**b**) the middle metal layer. Distributions of (**c**) the electric field in the x–y plane, (**d**) the electric field in the x–z plane, (**e**) the magnetic field in the x–y plane, and (**f**) the magnetic field in the y–z plane of the unit-cell structure in the proposed PMMA at 2.426 THz at a temperature of 280 K.

3.4. Tunability

Next, we studied the effects of different structural parameters on the absorption properties of the proposed PMMA with an external environment temperature of T = 280 K. Here, only four structural parameters were considered: the radius (R) of the top circle of the PMMA structure, thickness (t_1) of the top metal layer, thickness (H) of the InSb layer, and period length ($P_x = P_y$) of the cell structure. As the four different parameters vary, the corresponding change of resonant frequency could be interpreted by the equivalent resonance circuit theory with the LC model [49]. In the LC model, the resonance absorption frequency of the absorber is approximately given as $f_0 = 1/\left(2\pi\sqrt{LC}\right)$, where L and C present equivalent inductance and capacitance, respectively. The PMMA structure uses the top circular metal pattern layer, the metal layer, and the InSb dielectric layer as three inductors, respectively, and the gap between these two metal layers and the gap between the metal discs of the unit structure as two capacitors, which creates the capacitor-inductor resonator.

First, in the case where all the other parameters were unchanged, we analyzed the influence of the top circle radius R on the absorption performance of PMMA. The simulated absorption characteristic curve is shown in Figure 7a. It can be observed that as the radius R increases from 10 to 18 μm, the corresponding resonant frequency red-shifted from 2.844 to 2.35 THz with the absorption rate (~100%) unchanged. The red shift is mainly due to the increase in the equivalent inductance L and equivalent capacitance C of the absorber when R increases, resulting in a decrease in the resonant frequency f_0. Second, we analyzed the influence of thickness t on the absorption performance, as shown in Figure 7b. It can be observed that as thickness t_1 increases from 0.2 to 0.6 μm, the corresponding resonant frequency (2.426 THz) and absorption rate (99.9%) of PMMA are unchanged. Thus, t_1 does not affect the absorption performance. Third, we analyzed the influence of thickness H on the absorption performance, as shown in Figure 7c. As H increases from 3 to 6 μm, both the resonant frequency and absorption rate change. It can be observed from the enlarged image that the absorption peak frequency is red-shifted and the absorption rate is reduced from 99.9 to 84% with an increase in H. This is because, with the increase of H, the equivalent inductance of the InSb layer increases and the equivalent capacitance between the two metal plates decreases. Meanwhile, the equivalent capacitance decreases not as much as the inductance increases, resulting in a decrease in the resonant frequency, resulting in a decrease in the resonant frequency. Finally, we analyzed the influence of the period length ($P_x = P_y$) of the cell structure on the absorption performance, as shown in Figure 7d. With an increase in the period length from 48 to 60 μm, the absorption peak frequency slightly appeared blue-shifted, and the absorption rate decreased from 99.9 to 95.5%. The blue shift is due to the reduction in the coupling capacitance between the metal structures of adjacent absorber cells, resulting in a reduction in the total equivalent capacitance C. In summary, to ensure that the absorber has the best absorbing performance, we choose R = 16 μm, t_1 = 0.4 μm, H = 3 μm, $P_x = P_y$ = 50 μm as the structural parameters.

3.5. Temperature Sensor

We now focus on the effect of the external temperature on the absorption spectrum, which is an important feature in the design of temperature sensors. Based on the analysis in the second part, the complex permittivity ε of the InSb material is highly dependent on the external temperature T, which implies that the resonant absorption properties of PMMA can be dynamically tuned by changing T. Figure 8a shows the absorption spectra of the proposed PMMA at different external environmental temperatures T (260, 270, 280, 290, 300, and 310 K). It can be observed that the absorber has obvious absorption peaks at 2.047, 2.229, 2.426, 2.644, 2.883, and 3.141 THz, and all absorption rates can reach 99%. This shows that the designed absorber exhibits perfect absorbing performance at different temperatures, and the resonant frequency exhibits an obvious blue-shift phenomenon with an increase in temperature. We then studied the relationship between the resonance frequency of PMMA and the environmental temperature. As shown in Figure 8b, the fitted solid line

indicates a good linear relationship between the two parameters. This implies that the resonance absorption frequency shift Δf is proportional to the environmental temperature change ΔT. Therefore, the proposed PMMA could be used as a temperature sensor. We defined the temperature sensitivity as $S = \Delta f / \Delta T$, from which the temperature sensitivity of the proposed PMMA can be calculated as S = 21.9 GHz/K. For comparison, we quote previously reported temperature sensors in the same terahertz band, as shown in Table 1. It can be observed that the proposed PMMA has high sensitivity, high absorption coefficient, and stability.
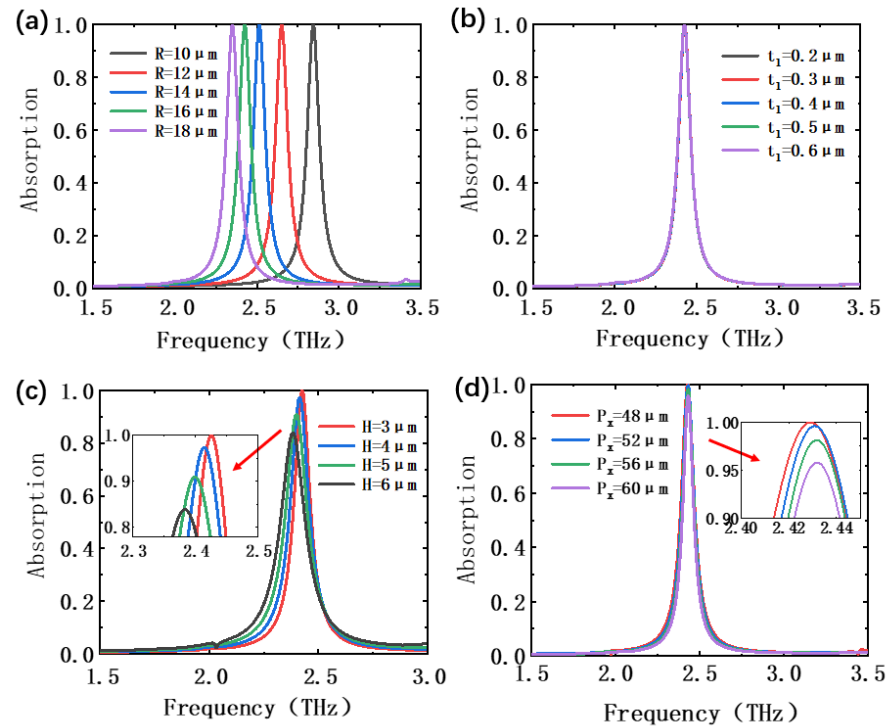

Figure 7. Simulated absorbance spectra for different structural parameters of the proposed PMMA under the environment temperature of T = 280 K: (**a**) the Radius R of the top metal circle, (**b**) the thickness t_1 of the metal layer, (**c**) the thickness H of the intermediate InSb layer, and (**d**) the period length $P_x = P_y$ of the cell structure.
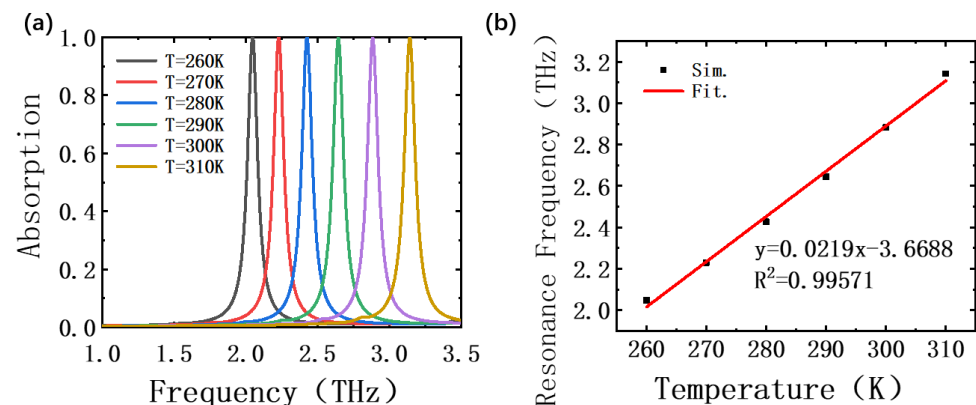

Figure 8. (**a**) Absorbance spectra of the designed PMMA with different temperatures T, (**b**) the simulated resonance frequencies (black squares), and the fitting curve (solid red line) as a function of external temperature T.

Table 1. Compare the previously reported sensor with the proposed sensor.

Reference	[23]	[29]	[44]	[27]	[28]	Proposed
Temperature sensitivity (GHz/K)	0.319	2.13	16.25	10.3	9.6	21.9
Maximum absorption rate (%)	99.8	99.9	98.7	99.9	99.9	99.9
Frequency band (THz)	0.01–0.3	1.6–2.0	1.5–2.0	0.4–2.2	1.1–1.6	1.0–3.5
Temperature range (K)	200–500	295–320	270–290	190–230	270–295	260–310
Polarization-insensitive	Yes	Yes	Yes	Yes	Yes	Yes
Wide angle absorption	No	No	No	-	No	Yes

Taking a further step, to improve the temperature sensitivity, we added a graphene layer between the InSb layer and the top metal layer. According to the analysis in the second section, because the optical properties of both graphene and InSb are strongly temperature-dependent, the resonant frequencies of the two materials shift in the same direction as the temperature changes. Therefore, according to the superposition, it can be inferred that the temperature sensitivity of PMMA can be further improved on the original basis. Figure 9a shows the absorption spectra of PMMA with the graphene film at different environmental temperatures T (260, 270, 280, 290, 300, and 310 K). It can be observed that the absorber has obvious absorption peaks at 1.815, 2.014, 2.232, 2.505, 2.762, and 3.023 THz, with absorption rates varying from 70 to 90%. The dramatic reduction in absorptivity is due to the impedance mismatch across the structure. As shown in Figure 9b, the temperature sensitivity is 24.4 GHz/K after linear fitting, increasing by 2.5 GHz/K, which is one of the highest thermal sensitivity values reported thus far.
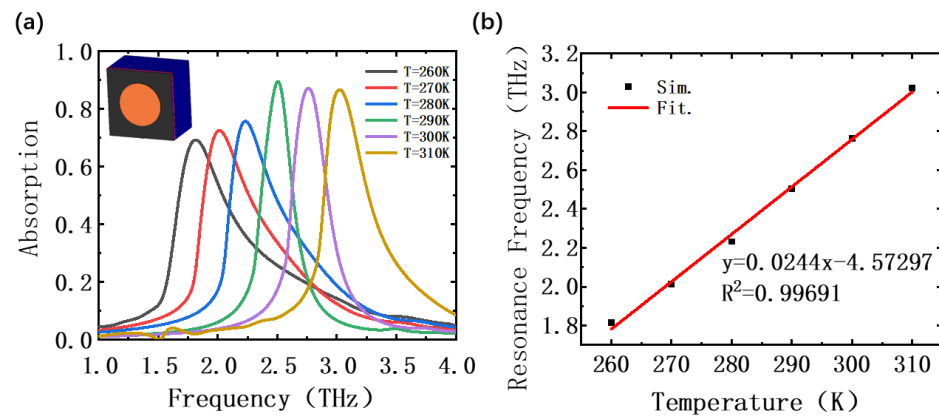

Figure 9. (**a**) Absorbance spectra of the designed PMMA based on added graphene layer with different temperature T, (**b**) the simulated resonance frequencies (black squares), and the fitting curve (solid red line) as a function of external temperature T.

3.6. Thermal Switch

Furthermore, the proposed PMMA can not only be applied as a temperature sensor but also as a thermal switch. Considering 270 K and 280 K as examples, it can be observed from Figure 10 that at 2.229 THz, the corresponding absorption rate at 270 K is 99.9%, whereas the corresponding absorption rate at 280 K is approximately 5%. Similarly, at 2.426 THz, the corresponding absorption rate at 280 K was 99.9%, whereas the corresponding absorption rate at 270 K was approximately 5%. We can define 2.229 THz as the standard point. When the absorption rate reaches 99%, it is defined as "on", otherwise, it is defined as "off". Thus, when the outside temperature reaches approximately 270 K, it is "on" and other temperatures are "off". In addition, in order to realize the thermal switch application, we design to use external conduction heating, placing the PMMA on cast aluminum heating plates and matching temperature control box to achieve precise temperature control. In conclusion, the proposed PMMA shows great potential for temperature applications.
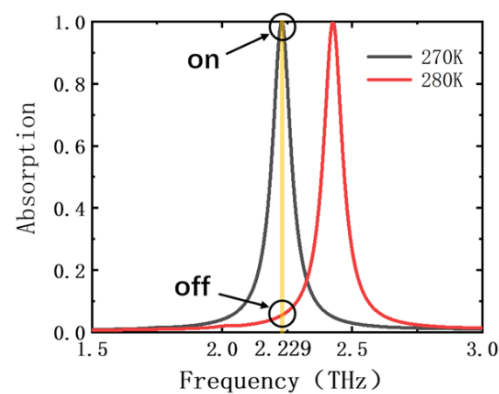
Figure 10. Absorption spectra of PMMA when external temperatures are 270 K and 280 K.

4. Conclusions

We used a THz metamaterial perfect absorber (PMMA) to realize a temperature sensor by exploiting the temperature sensitivity of InSb and graphene. The temperature sensitivity of our absorber reaches 21.9 GHz/K. In addition, the temperature sensitivity was further improved by adding graphene layers and changing the structural parameters to 24.4 GHz/K. It was demonstrated that the proposed PMMA has the characteristics of high-temperature sensitivity, high absorptivity, narrow bandwidth, polarization insensitivity, and wide-angle absorption. Therefore, the designed PMMA can be used as a highly sensitive passive wireless optical temperature sensor and a thermal switch.

Author Contributions: Y.W.: conceptualization, methodology, software, writing—original draft. Y.Q.: methodology, formal analysis. Y.Z.: software, formal analysis. T.L.: validation, writing—review and editing, supervision. F.Z.: software, writing—review and editing, supervision. All authors have read and agreed to the published version of the manuscript.

Institutional Review Board Statement: Not applicable.

Informed Consent Statement: Not applicable.

Data Availability Statement: Data is unavailable due to privacy.

Conflicts of Interest: The authors declare no conflict of interest.

References

1. Jha, K.; Singh, G. Terahertz planar antennas for future wireless communication: A technical review. *Infrared Phys. Technol.* **2013**, *60*, 71–80. [CrossRef]
2. Son, J.-H. *Terahertz Biomedical Science and Technology*; CRC Press: Boca Raton, FL, USA, 2014.
3. Mittleman, D.M. Twenty years of terahertz imaging. *Opt. Express* **2018**, *26*, 9417–9431. [CrossRef] [PubMed]
4. Singh, R.; Cao, W.; Al-Naib, I.; Cong, L.; Withayachumnankul, W.; Zhang, W. Ultrasensitive terahertz sensing with high-*Q* Fano resonances in metasurfaces. *Appl. Phys. Lett.* **2014**, *105*, 171101. [CrossRef]
5. Zheludev, N.I.; Kivshar, Y.S. From metamaterials to metadevices. *Nat. Mater.* **2012**, *11*, 917–924. [CrossRef]
6. Klimov, N.; Purdy, T.; Ahmed, Z. Towards replacing resistance thermometry with photonic thermometry. *Sens. Actuators A: Phys.* **2017**, *269*, 308–312. [CrossRef]
7. Guan, X.; Wang, X.; Frandsen, L.H. Optical temperature sensor with enhanced sensitivity by employing hybrid waveguides in a silicon Mach-Zehnder interferometer. *Opt. Express* **2016**, *24*, 16349–16356. [CrossRef]
8. Klimov, N.N.; Mittal, S.; Berger, M.; Ahmed, Z. On-chip silicon waveguide Bragg grating photonic temperature sensor. *Opt. Lett.* **2015**, *40*, 3934–3936. [CrossRef]
9. Dwivedi, R.; Kumar, A. Ultrahigh-sensitive temperature sensor based on modal interference in a metal-under-clad ridge waveguide with a polymer upper cladding. *Appl. Opt.* **2017**, *56*, 4685–4689. [CrossRef]
10. Kong, Y.; Wei, Q.; Liu, C.; Wang, S. Nanoscale temperature sensor based on Fano resonance in metal–insulator–metal waveguide. *Opt. Commun.* **2017**, *384*, 85–88. [CrossRef]

11. Vafapour, Z.; Alaei, H. Subwavelength Micro-Antenna for Achieving Slow Light at Microwave Wavelengths via Electromagnetically Induced Transparency in 2D Metamaterials. *Plasmonics* **2016**, *12*, 1343–1352. [CrossRef]

12. Jiang, L.; Yang, J.; Wang, S.; Li, B.; Wang, M. Fiber Mach–Zehnder interferometer based on microcavities for high-temperature sensing with high sensitivity. *Opt. Lett.* **2011**, *36*, 3753–3755. [CrossRef] [PubMed]

13. Hernández-Romano, I.; Monzón-Hernández, D.; Moreno-Hernández, C.; Moreno-Hernandez, D.; Villatoro, J. Highly sensitive temperature sensor based on a polymer-coated microfiber interferometer. *IEEE Photonics Technol. Lett.* **2015**, *27*, 2591–2594. [CrossRef]

14. Zhao, R.-A.; Lang, T.; Chen, J.; Hu, J. Polarization-maintaining fiber sensor for simultaneous measurement of the temperature and refractive index. *Opt. Eng.* **2017**, *56*, 057113. [CrossRef]

15. Karim, H.; Delfin, D.; Chavez, L.A.; Delfin, L.; Martinez, R.; Avila, J.; Rodriguez, C.; Rumpf, R.C.; Love, N.; Lin, Y. Metamaterial Based Passive Wireless Temperature Sensor. *Adv. Eng. Mater.* **2017**, *19*, 1600741. [CrossRef]

16. Aslinezhad, M. High sensitivity refractive index and temperature sensor based on semiconductor metamaterial perfect absorber in the terahertz band. *Opt. Commun.* **2020**, *463*, 125411. [CrossRef]

17. Keshavarz, A.; Zakery, A. Ultrahigh sensitive temperature sensor based on graphene-semiconductor metamaterial. *Appl. Phys. A* **2017**, *123*, 797. [CrossRef]

18. Radhouene, M.; Chhipa, M.K.; Najjar, M.; Robinson, S.; Suthar, B. Novel design of ring resonator based temperature sensor using photonics technology. *Photon- Sens.* **2017**, *7*, 311–316. [CrossRef]

19. Kim, H.-T.; Yu, M. Cascaded ring resonator-based temperature sensor with simultaneously enhanced sensitivity and range. *Opt. Express* **2016**, *24*, 9501–9510. [CrossRef]

20. Xia, H.; Lei, L.; Hong, W.; Xu, S. A novel $Ce^{3+}/Mn^{2+}/Eu^{3+}$ tri-doped GdF3 nanocrystals for optical temperature sensor and anti-counterfeiting. *J. Alloy. Compd.* **2018**, *757*, 239–245. [CrossRef]

21. Wang, X.; Liu, Q.; Bu, Y.; Liu, C.-S.; Liu, T.; Yan, X. Optical temperature sensing of rare-earth ion doped phosphors. *RSC Adv.* **2015**, *5*, 86219–86236. [CrossRef]

22. Hu, J.; Lang, T.; Shi, G.-H. Simultaneous measurement of refractive index and temperature based on all-dielectric metasurface. *Opt. Express* **2017**, *25*, 15241–15251. [CrossRef]

23. Li, W.; Cheng, Y. Dual-band tunable terahertz perfect metamaterial absorber based on strontium titanate (STO) resonator structure. *Opt. Commun.* **2020**, *462*, 125265. [CrossRef]

24. Li, D.; Huang, H.; Xia, H.; Zeng, J.; Li, H.; Xie, D. Temperature-dependent tunable terahertz metamaterial absorber for the application of light modulator. *Results Phys.* **2018**, *11*, 659–664. [CrossRef]

25. Sheta, E.; Choudhury, P.; Ibrahim, A.-B.M. Pixelated graphene-strontium titanate metamaterial supported tunable dual-band temperature sensor. *Opt. Mater.* **2021**, *117*, 111197. [CrossRef]

26. Ghafari, S.; Forouzeshfard, M.R.; Vafapour, Z. Thermo Optical Switching and Sensing Applications of an Infrared Metamaterial. *IEEE Sens. J.* **2019**, *20*, 3235–3241. [CrossRef]

27. Zou, H.; Cheng, Y. Design of a six-band terahertz metamaterial absorber for temperature sensing application. *Opt. Mater.* **2019**, *88*, 674–679. [CrossRef]

28. Luo, H.; Cheng, Y. Thermally tunable terahertz metasurface absorber based on all dielectric indium antimonide resonator structure. *Opt. Mater.* **2020**, *102*, 109801. [CrossRef]

29. Chen, F.; Cheng, Y.; Luo, H. Temperature Tunable Narrow-Band Terahertz Metasurface Absorber Based on InSb Micro-Cylinder Arrays for Enhanced Sensing Application. *IEEE Access* **2020**, *8*, 82981–82988. [CrossRef]

30. Luo, H.; Wang, X.; Qian, H. Tunable terahertz dual-band perfect absorber based on the combined InSb resonator structures for temperature sensing. *J. Opt. Soc. Am. B* **2021**, *38*, 2638. [CrossRef]

31. Zhong, M. Design and verification of a temperature-sensitive broadband metamaterial absorber based on VO2 film. *Opt. Mater.* **2020**, *109*, 110467. [CrossRef]

32. Hamouleh-Alipour, A.; Mir, A.; Farmani, A. Analytical Modeling and Design of a Graphene Metasurface Sensor for Thermo-Optical Detection of Terahertz Plasmons. *IEEE Sens. J.* **2020**, *21*, 4525–4532. [CrossRef]

33. Bonaccorso, F.; Sun, Z.; Hasan, T.; Ferrari, A.C. Graphene photonics and optoelectronics. *Nat. Photon-* **2010**, *4*, 611–622. [CrossRef]

34. Zhu, W.; Rukhlenko, I.D.; Premaratne, M. Graphene metamaterial for optical reflection modulation. *Appl. Phys. Lett.* **2013**, *102*, 241914. [CrossRef]

35. Zhao, X.; Yuan, C.; Zhu, L.; Yao, J. Graphene-based tunable terahertz plasmon-induced transparency metamaterial. *Nanoscale* **2016**, *8*, 15273–15280. [CrossRef] [PubMed]

36. Vakil, A.; Engheta, N. Transformation Optics Using Graphene. *Science* **2011**, *332*, 1291–1294. [CrossRef] [PubMed]

37. Koppens, F.H.L.; Chang, D.E.; de Abajo, F.J.G. Graphene Plasmonics: A Platform for Strong Light–Matter Interactions. *Nano Lett.* **2011**, *11*, 3370–3377. [CrossRef] [PubMed]

38. Han, J.; Lakhtakia, A. Semiconductor split-ring resonators for thermally tunable terahertz metamaterials. *J. Mod. Opt.* **2009**, *56*, 554–557. [CrossRef]

39. Zhu, J.; Han, J.; Tian, Z.; Gu, J.; Chen, Z.; Zhang, W. Thermal broadband tunable Terahertz metamaterials. *Opt. Commun.* **2011**, *284*, 3129–3133. [CrossRef]

40. Howells, S.C.; Schlie, L.A. Transient terahertz reflection spectroscopy of undoped InSb from 0.1 to 1.1 THz. *Appl. Phys. Lett.* **1996**, *69*, 550–552. [CrossRef]

41.　Rode, D.L. Electron transport in insb, inas, and inp. *Phys. Rev. B* **1971**, *3*, 3287. [CrossRef]

42.　Shi, C.; He, X.; Liu, F.; Lin, F.; Zhang, H. Investigation of graphene-supported tunable asymmetric terahertz metamaterials. *J. Opt. Soc. Am. B* **2018**, *35*, 575–581. [CrossRef]

43.　Sánchez-Gil, J.A.; Rivas, J.G. Thermal switching of the scattering coefficients of terahertz surface plasmon polaritons impinging on a finite array of subwavelength grooves on semiconductor surfaces. *Phys. Rev. B* **2006**, *73*, 205410. [CrossRef]

44.　Oszwałldowski, M.; Zimpel, M. Temperature dependence of intrinsic carrier concentration and density of states effective mass of heavy holes in InSb. *J. Phys. Chem. Solids* **1988**, *49*, 1179–1185. [CrossRef]

45.　Halevi, P.; Ramos-Mendieta, F. Tunable photonic crystals with semiconducting constituents. *Phys. Rev. Lett.* **2000**, *85*, 1875. [CrossRef]

46.　Hanson, G.W. Dyadic Green's functions and guided surface waves for a surface conductivity model of graphene. *J. Appl. Phys.* **2008**, *103*, 064302. [CrossRef]

47.　Falkovsky, L.A.; Pershoguba, S. Optical far-infrared properties of a graphene monolayer and multilayer. *Phys. Rev. B* **2007**, *76*, 153410. [CrossRef]

48.　Islam, M.; Sultana, J.; Biabanifard, M.; Vafapour, Z.; Nine, M.; Dinovitser, A.; Cordeiro, C.; Ng, B.-H.; Abbott, D. Tunable localized surface plasmon graphene metasurface for multiband superabsorption and terahertz sensing. *Carbon* **2019**, *158*, 559–567. [CrossRef]

49.　Engheta, N. Circuits with Light at Nanoscales: Optical Nanocircuits Inspired by Metamaterials. *Science* **2007**, *317*, 1698–1702. [CrossRef] [PubMed]